

# AI Algorithm-Based Two-Stage Optimal Design Methodology of High-Efficiency CLLC Resonant Converters for the Hybrid AC–DC Microgrid Applications

Bin Zhao <sup>✉</sup>, Member, IEEE, Xin Zhang <sup>✉</sup>, Member, IEEE, and Jingjing Huang <sup>✉</sup>, Member, IEEE

**Abstract**—Thanks to the advantages of high power density and the capacity of bidirectional power transfer, the CLLC resonant converter is widely used in the hybrid ac–dc microgrid as a dc transformer to interlink the ac and dc bus. Since the voltages of ac and dc bus are controlled by the energy management system, the CLLC resonant converter operates under open-loop condition, which means the switching frequency and duty cycle are fixed. As a result, in the hybrid ac–dc microgrid applications, for the CLLC converter, the main concern is not the voltage regulation but the conversion efficiency. This paper focuses on the total power loss optimization and the magnetic design of the CLLC resonant converter based on artificial intelligence (AI) algorithm. In order to optimize the total power loss, an AI algorithm-based two-stage optimal design method is proposed. In the first stage, the total power loss, including the driving loss, turn-OFF loss, conduction loss of the switches, the power loss of the resonant capacitances, and copper and core loss of the transformer are optimized by the proposed AI algorithm, GA+PSO, and the optimal parameters, including the leakage inductances ( $L_{r1}$  and  $L_{r2}$ ), magnetizing inductance ( $L_m$ ), and resonant capacitances ( $C_{r1}$  and  $C_{r2}$ ) are derived. In the second stage, the optimal leakage inductances and magnetizing inductance are realized by setting proper distance between the primary winding and the secondary winding ( $d_w$ ), and the thickness of the air gap ( $d_a$ ). As for the magnetic design, in this paper, the leakage inductances of a planar transformer are used as the resonant inductances. The equations of  $d_w$  and  $d_a$  to achieve the optimal leakage inductances and magnetizing inductance are derived. Both the proposed optimal design

method and the equations of  $d_w$  and  $d_a$  are validated by simulations and experiments.

**Index Terms**—Artificial intelligence (AI) algorithm, CLLC resonant converter, hybrid ac–dc microgrid, magnetic design, total power loss.

## I. INTRODUCTION

WITH MORE and more renewable energy sources, such as the PV panels, wind turbines, integrated into the power system, the hybrid ac–dc microgrid, which includes the dc sub-microgrid and ac sub-microgrid, is becoming popular [1]–[3]. Due to the integration of the ac–dc sources and the loads, the bus conversion system is required to interlink the ac and dc bus. The typical structure of a hybrid ac–dc microgrid is shown in Fig. 1 [4], where a bidirectional interlinking converter (BIC) and a dc transformer is used to interlink between the ac and dc bus.

The BIC is a bidirectional power converter [5]. When the power flows from dc to ac bus, BIC works as an inverter; when the power flows from ac to dc bus, BIC works as a rectifier. As for the dc transformer, the symmetrical CLLC resonant converters (see Fig. 2) and dual active bridge (DAB) converters are usually applied [6]–[8], because of their advantages such as high power density, high efficiency, buck and boost capability, and bidirectional power transfer [9]. However, for the DAB converters, under light load conditions, the advantage of zero voltage switching (ZVS) will disappear. In contrast, the symmetrical CLLC resonant converter can achieve ZVS for the primary main switches and zero current switching (ZCS) for the secondary rectifiers [9].

In order to achieve soft switching under all load conditions, this paper focuses on the symmetrical CLLC resonant converter as the dc transformer in the hybrid ac–dc microgrid applications.

Previous research on the symmetrical CLLC resonant converter can be reviewed as topology research [10]–[13], controls [10], [14], and the magnetic design [14]–[20]. The working principles and equations of the circuit parameters are explained in detail in [10] and [11]. In addition, a voltage gain-based design methodology for the CLLC resonant converter is proposed [10]. In [12], the robust circuit parameters design of the CLLC resonant converter with the open-loop control for the optimal power transmission and voltage regulation ability is proposed. In [13],

Manuscript received August 30, 2018; revised December 16, 2018; accepted January 9, 2019. Date of publication February 20, 2019; date of current version July 31, 2019. This work was supported by Singapore ACRF Tier 1 under Grant RG 85/18, as well as in part by the start-up grant (SCOPES) of Professor Xin Zhang. (Corresponding author: Xin Zhang.)

B. Zhao was with the Nanyang Technological University, Singapore 639798. He is now with the Space Travelling-Wave Tube Research & Development Center, Institute of Electronics, Chinese Academy of Sciences, Beijing 100049, China, and also with the University of Chinese Academy of Sciences, Beijing 100049, China (e-mail: binzhao.icas@foxmail.com).

X. Zhang and J. Huang are with the Department of Electrical and Electronic Engineering, Nanyang Technological University, Singapore 639798 (e-mail: jackzhang@ntu.edu.sg; hjj7759@163.com).

Color versions of one or more of the figures in this paper are available online at <http://ieeexplore.ieee.org>.

Digital Object Identifier 10.1109/TIE.2019.2896235

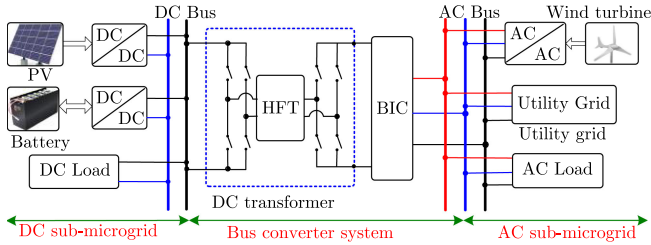


Fig. 1. Typical structure of a hybrid ac-dc microgrid.

the conventional *CLLC* resonant converter is integrated with a buck/boost converter, where high voltage gain can be achieved by pulsewidth modulation. As for the control strategies, in [10], an intelligent digital control algorithm is proposed to regulate output voltage and to control bidirectional power conversions. In [14], a linear state-space model for a phase-controlled *CLLC* resonant converter is derived. This model can be used for fast simulations, prediction of the state variables with large signal variation. As for the magnetic components design, as shown in Fig. 2, there are two resonant inductances and a transformer in a *CLLC* resonant converter. Besides the conventional way, where two separate inductances are used [9], the leakage inductances are used as the resonant inductances [15]–[17]. In [18], a novel six-layer PCB winding transformer is proposed for a three-phase *CLLC* resonant converter, where all the resonant inductors are integrated into a transformer. In [19], a high frequency transformer is designed for modular power conversion with consideration of insulation, efficiency, and power density.

In the hybrid ac-dc microgrid applications, since the voltage regulations of the ac and dc bus are achieved by the energy management system (EMS) [7], the *CLLC* resonant converter operates under the open-loop condition. The main function of the *CLLC* resonant converter is the power transmission with high efficiency [12]. As a result, the challenge for the *CLLC* resonant converter is not the voltage regulation but the conversion efficiency. In order to achieve high efficiency, the total power loss of the converter needs to be further optimized. Previous researches on the *CLLC* resonant converter covered the power loss analysis [13], [19], however, the total power loss optimization is the most challenging because of the multiple variables and their internal couplings. As a result, the research on the total power loss optimization is rarely reported.

From the perspective of the magnetic design in the *CLLC* resonant converter, using the leakage inductances as the resonant inductances is the general way to improve the power density [15], [16], because the discrete inductors are not required. However, the general equations of the distance between the primary winding and secondary winding ( $d_w$ ), and the thickness of the air gap ( $d_a$ ) to design the specific leakage inductances and magnetizing inductance, with consideration of the thicknesses of the conductors and insulations are not reported.

In this paper, the AI algorithm is used to solve the problem caused by the multiple variables and internal couplings in the *CLLC* resonant converter. Nowadays, the metaheuristic algorithms, including the single solution-based algorithms, such as, Simulated Annealing (SA) algorithm; and the population-based algorithms, such as Ant Colony (ACO) algorithm, Bee Colony

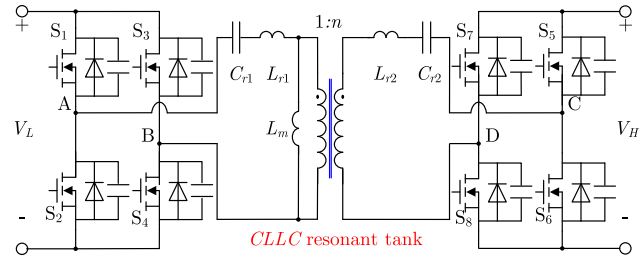


Fig. 2. Typical symmetrical *CLLC* resonant converter as a dc transformer.

(BCO) algorithm, Artificial Immune System (AIS) algorithm, Genetic Algorithm (GA), and Particle Swarm Optimization (PSO), are increasingly popular in optimization problems [21]–[34]. Due to advantages of simplicity, universality, and robustness, the single-solution based, SA algorithm is utilized for voltage stability constrained reactive power planning [22], and parameter identification of energetic hysteresis model [23]. However, the convergence speed of the SA algorithm is relatively slow, which means long execution time. In addition, the performance of the algorithm is closely related with the initial parameters. As for the ACO algorithm, as a general population-based stochastic optimization approach, it has been used to solve combinatorial optimization problems, such as the control of induction motors [24], traveling salesman problem (TSP) [25]. However, similar to SA algorithm, the convergence speed and the quality of the solutions are very sensitive to the initial parameters. In addition, lots of computation is required. As another population-based search algorithm, the BCO algorithm has been used for the Sheppard–Taylor PFC converter [26], optimal distributed generation allocation, and sizing in distribution systems [27]. However, from the nature of the algorithm, BCO algorithm is a local optimal algorithm. Furthermore, the execution time is still long, especially when solving large-scale optimization problems. Thanks to the high information processing and evolution capabilities, the AIS algorithm is widely applied in pattern recognition and classification problems [28]. However, the robustness of the algorithm is heavily affected by the antibody levels.

Recently, the PSO algorithm is widely applied due to its advantages of simplicity, high accuracy, and high convergence speed [29]–[31]. However, the performance of the PSO algorithm, such as the convergence speed and the execution time is heavily affected by the parameter settings. In addition, the premature problem further limits the algorithm performance. Complimentary to PSO algorithm, GA algorithm can overcome the premature problem and be easily integrated with other algorithms [32]–[34]. In this paper, in order to achieve high accuracy, high convergence speed, and short execution time, a GA+PSO algorithm is proposed for the total power loss optimization of the *CLLC* resonant converter, where the GA algorithm is executed to extract the optimal parameters for the PSO algorithm. With the optimal parameters from GA, the PSO is expected to keep the advantages while overcoming the shortcomings.

In general, the purposes of this paper can be summarized as total power loss optimization and its corresponding magnetic design: *From the view of the total power loss optimization, based*

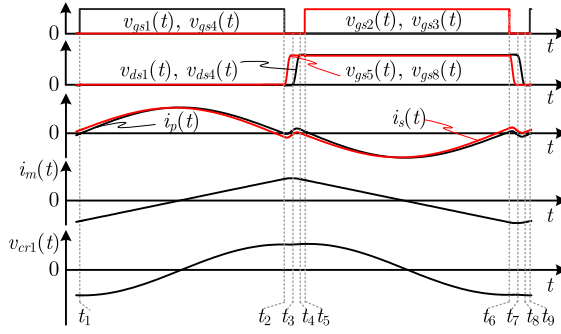


Fig. 3. Typical ZVS & ZCS waveforms of a CLLC resonant converter.

on the proposed GA+PSO algorithm, this paper aims to minimize the total power loss of the symmetrical CLLC resonant converter as a dc transformer, with full consideration of switching loss, conduction loss of the switches, resonant capacitance loss, copper loss, and core loss of the transformer. First of all, the working principles of the CLLC resonant converter and the calculations of the main parameters are investigated. Then, a GA+PSO-based two-stage optimal design method is proposed to minimize the total power loss of the CLLC resonant converter: Stage-1 is a GA+PSO algorithm to optimize the main parameters and Stage-2 utilizes the hybrid electromagnetic analysis approach to design the transformer to achieve the optimized parameters derived from AI algorithm. *From the view of the magnetic design*, this paper proposes a method to design the optimal leakage inductances and magnetizing inductance. The equations of  $d_w$  and  $d_a$  to achieve the optimal leakage inductances and magnetizing inductance are derived.

The rest of this paper is organized as follows. In Section II, the working principles and the calculations of the main parameters of the CLLC resonant converter are investigated. Section III is the main part of the paper, mainly focusing on the AI-based two-stage optimal design method: First, the equation of the total power loss is derived for the further optimization; then, a hybrid AI algorithm, GA+PSO, is proposed to optimize the total power loss, which is the first stage. After that, in order to achieve the desired optimal parameters of the optimized transformer, a planar transformer for the CLLC resonant converter is designed, where the leakage inductances are utilized as the resonant inductances. In Section IV, the proposed two-stage optimal design method and the equations of  $d_w$  and  $d_a$  are validated by simulations and experiments. Section V concludes this paper.

## II. WORKING PRINCIPLES AND THE CIRCUIT ANALYSIS OF THE CLLC RESONANT CONVERTER IN HYBRID AC-DC MICROGRID APPLICATIONS

The working principles and the calculations of the open-loop CLLC resonant converter are analyzed in this section. In order to achieve high efficiency, the CLLC resonant converter should operate with 50% duty cycle [35]. In addition, in order to achieve ZVS and ZCS, the switching frequency ( $f_s$ ) should be slightly lower than the resonant frequency ( $f_r$ ) between  $C_{r1}$  and  $L_{r1}$ . The ZVS and ZCS waveforms of CLLC resonant converters are shown in Fig. 3.

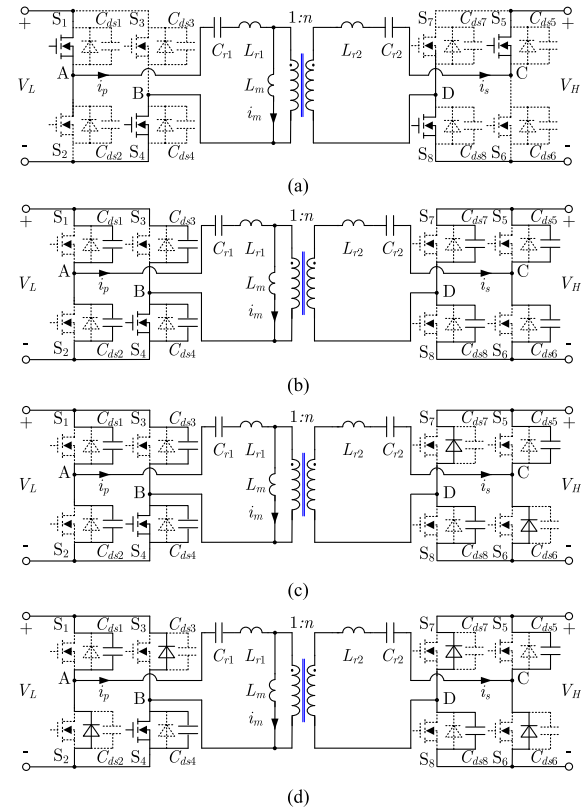


Fig. 4. Equivalent circuit. (a) Mode 1. (b) Mode 2. (c) Mode 3. (d) Mode 4.

### A. Working Principles of the Open-Loop CLLC Resonant Converter as a DC Transformer

The main waveforms of interest are as follows:

- 1) The driving signals of  $S_1$  and  $S_4$ ,  $v_{gs1(4)}$ , same as  $S_5$  and  $S_8$ ; the driving signals of  $S_2$  and  $S_3$ ,  $v_{gs2(3)}$ , same as  $S_6$  and  $S_7$ ,  $v_{gs5(7)}$ ;
- 2) the voltage across the parasitic capacitor of  $S_1$ ,  $v_{ds1}(t)$ , same as  $v_{ds4}(t)$ ; the voltage across the parasitic capacitor of  $S_5$ ,  $v_{ds5}(t)$ , same as  $v_{ds8}(t)$ ;
- 3) the current on the primary side,  $i_p(t)$ ; the current on the secondary side,  $i_s(t)$ ;
- 4) the magnetizing current,  $i_m(t)$ ;
- 5) the voltage across the series capacitor ( $C_{r1}$ ),  $v_{Cr1}(t)$ ;
- 6) The assumptions are made in the analysis as follows:
  - a) the input voltage ( $V_L$ ) and output voltage ( $V_H$ ) are constant;
  - b) all the components are ideal (lossless).

*Mode 1* ( $t_1$ ,  $t_2$ ): the waveforms of Mode 1 (from  $t_1$  to  $t_2$ ) are shown in Fig. 3 and the equivalent circuit of Mode 1 is shown in Fig. 4(a). Prior to Mode 1, the primary current,  $i_p(t)$ , flows through the body diodes of  $S_1$  and  $S_4$  while the secondary current,  $i_s(t)$ , flows through the body diodes of  $S_5$  and  $S_8$ . As a result, the voltages of  $S_1$ ,  $S_4$ ,  $S_5$ , and  $S_8$ ,  $v_{ds1}(t)$ ,  $v_{ds4}(t)$ ,  $v_{ds5}(t)$  and  $v_{ds8}(t)$  are clamped to 0. At  $t_1$ ,  $S_1$ ,  $S_4$ ,  $S_5$ , and  $S_8$  are turned-ON and ZVS of  $S_1$ ,  $S_4$ ,  $S_5$ , and  $S_8$  is achieved.

The resonance begins among  $L_{r1}$ ,  $C_{r1}$ ,  $L_{r2}$ , and  $C_{r2}$  and power is transferred from the primary side to the load. When

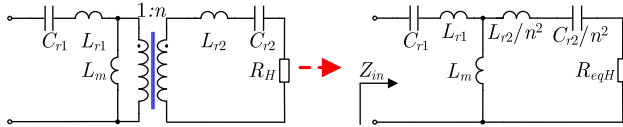


Fig. 5. Derivation of equivalent input impedance  $Z_{in}$ .

the turn-ON time of  $S_1$ ,  $S_4$ ,  $S_5$ , and  $S_8$  reaches  $T_r/2$ , where  $T_r$  is the resonant period between  $L_{r1}$  and  $C_{r1}$ ,  $S_1$ ,  $S_4$ ,  $S_5$ , and  $S_8$  will be turned-OFF. Mode 1 ends.

**Mode 2 ( $t_2$ ,  $t_3$ ):** the waveforms of Mode 2 (from  $t_2$  to  $t_3$ ) are shown in Fig. 3 and the equivalent circuit of Mode 2 is shown in Fig. 4(b). A complex resonance begins among  $L_{r1}$ ,  $C_{r1}$ ,  $L_{r2}$ ,  $C_{r2}$ ,  $L_m$ , and all the parasitic capacitances of the switches. The voltages of  $S_6$  and  $S_7$  will decrease while the voltages of  $S_5$  and  $S_8$  will increase. When the voltages of  $S_5$  and  $S_8$  increase to  $V_H$ , the body diodes of  $S_6$  and  $S_7$  will turn-ON, Mode 2 ends.

**Mode 3 ( $t_3$ ,  $t_4$ ):** the waveforms of Mode 3 are shown in Fig. 3 (from  $t_3$  to  $t_4$ ) and the equivalent circuit of Mode 3 is shown in Fig. 4(c). In Mode 3, the body diodes of  $S_6$  and  $S_7$  are ON. The voltages of  $S_2$  and  $S_3$  will decrease while the voltages of  $S_1$  and  $S_4$  will increase. When the voltages of  $S_2$  and  $S_3$  are 0, the body diodes of  $S_2$  and  $S_3$  will turn-ON. Mode 3 ends.

**Mode 4 ( $t_4$ ,  $t_5$ ):** the waveforms of Mode 4 (from  $t_4$  to  $t_5$ ) are shown in Fig. 3 and the equivalent circuit of Mode 4 is shown in Fig. 4(d). In Mode 4, the body diodes of  $S_2$ ,  $S_3$ ,  $S_6$ , and  $S_7$  are ON. As a result, the voltages of  $S_2$ ,  $S_3$ ,  $S_6$ , and  $S_7$  are clamped to 0. When  $S_2$ ,  $S_3$ ,  $S_6$ , and  $S_7$  are turned-ON, Mode 4 ends and ZVS of  $S_2$ ,  $S_3$ ,  $S_6$ , and  $S_7$  is achieved.

The second half period is symmetrical with the first half period, with Mode 5 similar to Mode 1 from  $t_5$  to  $t_6$ ; Mode 6 similar to Mode 2 from  $t_6$  to  $t_7$ , Mode 7 similar to Mode 3 from  $t_7$  to  $t_8$ , and Mode 8 similar to Mode 4 from  $t_8$  to  $t_9$ .

## B. Circuit Analysis of the CLLC Resonant Converter

The equations of the voltage gain ( $V_H/V_L$ ), the rms values of  $i_p(t)$  and  $i_s(t)$ ,  $I_{p,\text{rms}}$  and  $I_{s,\text{rms}}$ ; the peak flux density ( $B_{pk}$ ) and the switching period,  $T_s$  are summarized as follows:

### 1) Voltage gain [6]

$$V_H/V_L = n \quad (1)$$

where  $n$  is the turns ratio of the transformer.

### 2) rms values of $i_p(t)$ : $I_{p,\text{rms}}$

The equivalent circuit to derive the impedance  $Z_{in}$  is shown in Fig. 5.  $R_H$  is the load of the converter in the secondary side, which can be calculated by

$$R_H = 8V_H^2/(\pi^2 P_H) \quad (2)$$

where  $P_H$  is the output power.

$R_{eqH}$  is the load referred to the primary side, which can be calculated by

$$R_{eqH} = 8V_H^2/(\pi^2 n^2 P_H). \quad (3)$$

In a symmetrical CLLC resonant converter

$$L_{r2} = L_{r1}/n^2 \quad (4a)$$

$$C_{r2} = n^2 C_{r1}. \quad (4b)$$

The impedance,  $Z_{in}$ , as shown in Fig. 5, can be calculated by

$$Z_{in} = \sqrt{R_{eq}^2 + X_{eq}^2} \quad (5)$$

where  $R_{eq}$  is the real part and  $X_{eq}$  is the imaginary part.

$R_{eq}$  and  $X_{eq}$  can be calculated by

$$R_{eq} = \omega_s^4 R_{eqH} L_m^2 C_{r1}^2 / \omega_s^2 R_{eqH}^2 C_{r1}^2 + (\omega_s^2 C_{r1} L_{r1} + \omega_s^2 C_{r1} L_m - 1)^2 \quad (6a)$$

$$X_{eq} = \frac{C_{r1}^3 L_{r1} (L_{r1} + L_m) (L_{r1} + 2L_m) \omega_s^6 + \sigma_2 \omega_s^4 + \sigma_3 \omega_s^2 - 1}{\omega_s C_{r1} [\omega_s^2 R_{eqH}^2 C_{r1}^2 + (\omega_s^2 C_{r1} L_{r1} + \omega_s^2 C_{r1} L_m - 1)^2]} \quad (6b)$$

where  $\omega_s$  is the angular frequency, corresponding to  $f_s$ .

$\sigma_2$  and  $\sigma_3$  can be calculated by

$$\sigma_2 = C_{r1}^2 [(L_{r1} + L_m) (R_H^2 C_{r1} - L_{r1} - L_m) - 4L_{r1} L_m - 2L_{r1}^2 - L_m^2] \quad (7a)$$

$$\sigma_3 = 3C_{r1} (L_{r1} + L_m) - R_H^2 C_{r1}^2 \quad (7b)$$

$I_{p,\text{rms}}$  can be calculated by

$$I_{p,\text{rms}} = V_L / \sqrt{2} Z_{in} \quad (8)$$

$I_{s,\text{rms}}$  can be calculated by

$$I_{s,\text{rms}} = V_L / \sqrt{2n} Z_{in}. \quad (9)$$

### 3) Peak magnetizing current $I_{m,pk}$ and peak flux density $B_{pk}$

Under steady state, the magnetizing current,  $i_m(t)$ , is symmetrical. As a result,  $I_{m,pk}$  can be calculated by

$$I_{m,pk} = (V_L T_s) / (4L_m). \quad (10)$$

The peak magnetic flux density,  $B_{pk}$ , which will be used to calculate the core loss of the transformer can be calculated by

$$B_{pk} = (L_m I_{m,pk}) / (n_p A_e) \quad (11)$$

where  $n_p$  is the number of turns in the primary winding,  $A_e$  is the cross-sectional area of the magnetic core.

### 4) Switching period ( $T_s$ )

Based on the analysis of the working principles, the switching period of the CLLC resonant converter is

$$T_s = T_r + 2T_d \quad (12)$$

where  $T_d$  is the dead time ( $T_d = t_5 - t_2$ ).

## C. Conditions of ZVS and ZCS

As shown in Fig. 3, before  $S_1$ ,  $S_4$ ,  $S_5$ , and  $S_8$  are turned-ON,  $i_p(t)$  and  $i_s(t)$  are discharging  $C_{ds1}$ ,  $C_{ds4}$ ,  $C_{ds5}$ , and  $C_{ds8}$ ,

which makes the ZVS condition of  $S_1$ ,  $S_4$ ,  $S_5$ , and  $S_8$ . Similarly,  $S_2$ ,  $S_3$ ,  $S_6$ , and  $S_7$  can also operate under ZVS condition due to  $i_p(t)$  and  $i_s(t)$ . The dead time considering ZVS condition is [10]

$$T_d \geq 16C_{oss}f_sL_m \quad (13)$$

where  $C_{oss}$  is the output capacitance of the switches. In order to achieve ZVS while keeping high efficiency,  $T_d$  is selected as the lower limiting value of the above equation, which is

$$T_d = 16C_{oss}f_sL_m. \quad (14)$$

In order to achieve the soft commutation of the rectifiers, duration of Modes 3 and 4 should be reserved, therefore

$$f_s \leq f_r. \quad (15)$$

It is worthy to mention that, with the conditions of ZVS of the main switches and the rectifiers, the switching loss is reduced. However, the total power loss still includes the driving loss, conduction loss of the switches, power loss of the resonant capacitances, copper loss, and core loss of the transformer. As a result, the total power loss of the converter needs further optimization. Therefore, in Section III, the total power loss of the *CLLC* resonant converter will be optimized by a two-stage optimized method.

### III. AI-BASED HIGH EFFICIENCY ORIENTED TWO-STAGE OPTIMAL DESIGN METHOD OF *CLLC* RESONANT CONVERTERS IN THE HYBRID AC-DC MICROGRID

In this section, an AI algorithm-based two-stage optimal design methodology is proposed for the total power loss optimization of the open-loop *CLLC* resonant converter. The equation of the total power loss in the *CLLC* resonant converter is derived in the first part. In the second part, the proposed AI-based two-stage optimal design methodology is elaborated to derive the optimal transformer parameters, which is the first stage of the optimization procedure. In the third part, a hybrid electromagnetic analysis is carried out to design the planar transformer with the leakage inductances as the resonant inductances derived from the AI algorithm, which is the second stage of the optimization procedure.

#### A. Preliminary of the AI-Based Two-Stage Optimal Design Method: Total Power Loss Equation of the *CLLC* Converter

As discussed before, in the *CLLC* resonant converter, although ZVS of the switches are achieved, the total power loss ( $P_{tot}$ ) still includes the driving loss of the main switches ( $P_{M\_dr}$ ) and the rectifiers ( $P_{R\_dr}$ ), the turn-OFF loss of the main switches ( $P_{M\_off}$ ) and the rectifiers ( $P_{R\_off}$ ), the conduction loss of the main switches ( $P_{M\_on}$ ) and the rectifiers ( $P_{R\_on}$ ), copper loss of the transformer ( $P_{T\_Cu}$ ), core loss of the transformer ( $P_{T\_Fe}$ ), and the power loss of the resonant capacitance ( $P_{Cr}$ ). Therefore, the  $P_{tot}$  can be expressed as

$$\begin{aligned} P_{tot} = & P_{M\_dr} + P_{R\_dr} + P_{M\_on} + P_{R\_on} + P_{T\_Cu} \\ & + P_{T\_Fe} + P_{Cr}. \end{aligned} \quad (16)$$

The detailed expression of  $P_{M\_dr}$ ,  $P_{R\_dr}$ ,  $P_{M\_off}$ ,  $P_{R\_off}$ ,  $P_{M\_on}$ ,  $P_{R\_on}$ ,  $P_{T\_Fe}$ ,  $P_{T\_Cu}$ , and  $P_{Cr}$  can be derived as follows:

- 1) *Driving loss of main switches (rectifiers):* The driving loss can be calculated by

$$P_{M(R)\_dr} = 4Q_{M(R)g}V_{M(R)gs}f_s \quad (17)$$

where  $Q_{M(R)g}$  and  $V_{M(R)gs}$  are the gate charge and the driving voltage of the main switches or rectifiers.

- 2) *Turn-OFF loss of the main switches (rectifiers):* Considering that the turn-OFF time is very short, the magnetizing current,  $i_m(t)$ , can be treated as constant during the turn-OFF process. Assuming the current through  $S_1$  and  $S_4$  is linearly reduced from  $I_{m,pk}$  to 0 in the dead time duration,  $T_d$ . The turn-OFF current is expressed as

$$i_{p\_off}(t) = I_{m,pk}(1 - t/T_d). \quad (18)$$

The voltage across  $S_1$  and  $S_4$  during the turn-OFF process may be obtained by

$$v_{M\_off}(t) = I_{m,pk}/(4C_{oss}T_d)t^2. \quad (19)$$

The turn-OFF loss of the main switches is calculated by

$$P_{M\_off} = (I_{m,pk}^2 T_d^2 f_s)/(12C_{oss}). \quad (20)$$

Similarly, the turn-OFF loss of the rectifiers can be calculated by

$$P_{R\_off} = (I_{m,pk}^2 T_d^2 f_s)/(12n^2 C_{oss}). \quad (21)$$

Therefore, the total turn-OFF loss of the main switches and the rectifiers is

$$P_{S\_off} = (1 + 1/n^2)(I_{m,pk}^2 T_d^2 f_s)/(12C_{oss}). \quad (22)$$

- 3) *Conduction loss of main switches (rectifiers):* The conduction loss can be calculated by

$$P_{M(R)\_on} = 2I_{p(s),rms}^2 R_{M(R)\_on} \quad (23)$$

where  $R_{M(R)\_on}$  is the on-resistance of the main switches (rectifiers).  $I_{p(s),rms}$  is the corresponding rms value of the resonant current, which can be found from (8) and (9).

- 4) *Copper loss of the transformer:* The copper loss of the transformer can be found by

$$P_{T\_Cu} = I_{p,rms}^2 R_{T\_ac} \quad (24)$$

where  $R_{T\_ac}$  is the ac resistance of the transformer referred to the primary winding.

- 5) *Core loss of the transformer ( $P_{T\_Fe}$ ):* The core loss can be calculated based on Steinmetz equation

$$P_{T\_Fe} = k_c f_s^\alpha (B_{pk})^\beta V_e \quad (25)$$

where  $B_{pk}$  can be found by (11).  $k_c$ ,  $\alpha$ , and  $\beta$  can be found from the datasheet of the magnetic material.  $V_e$  is the volume of the core.

- 6) *Power loss of the resonant capacitances:* The equivalent serial resistor (ESR) of the resonant capacitance can be

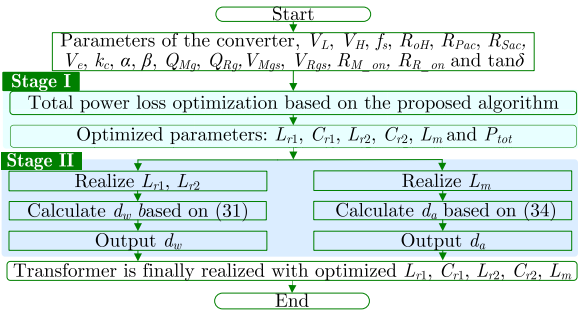


Fig. 6. Proposed two-stage optimal design methodology.

calculated by

$$R_{Cr1(2)} = \tan \delta / (2\pi f_s C_{r1(2)}) \quad (26)$$

where  $\delta$  is the dielectric loss angle.

As a result, the power loss of the resonant capacitance can be calculated by

$$P_{Cr1(2)} = I_{p(s),rms}^2 \tan \delta / (2\pi f_s C_{r1(2)}). \quad (27)$$

Based on the above analysis, combining (17), (22)–(25), and (27), the total power loss of a CLLC resonant converter is

$$P_{tot} =$$

$$\begin{aligned} & 4Q_{Mg}V_{Mgs}f_s + 4Q_{Rg}V_{Rgs}f_s + I_{p,rms}^2 [2R_{M\_on} \\ & + R_{T\_ac} + \tan \delta / (2\pi f_s C_{r1})] + I_{s,rms}^2 [2R_{R\_on} \\ & + \tan \delta / (2\pi f_s C_{r2})] \\ & + k_c f_s^\alpha [(L_m I_{m,pk}) / (n_p A_e)]^\beta V_e. \end{aligned} \quad (28)$$

### B. Proposed AI-Based (GA+PSO) Two-Stage Optimal Design Methodology for the CLLC Resonant Converter

The flowchart of the proposed two-stage optimal design method is shown in Fig. 6. At the beginning of the proposed two-stage optimal design, the magnetic core is selected according to the power rating and the switching frequency. The proposed optimal design method performs the following two stages:

*Stage 1:* Total power loss optimization based on the proposed AI algorithm (GA+PSO)

The total power loss is optimized based on the proposed GA+PSO algorithm to derive the optimal  $L_{r1}$ ,  $C_{r1}$ ,  $L_{r2}$ ,  $C_{r2}$ ,  $L_m$ , and  $P_{tot}$ , which will be used to design the transformer.

*Stage 2:* Design of the transformer to achieve the optimal  $L_{r1}$ ,  $L_{r2}$ , and  $L_m$  derived from the AI algorithm based on hybrid electromagnetic analysis.

When  $L_{r1}$ ,  $C_{r1}$ ,  $L_{r2}$ ,  $C_{r2}$ ,  $L_m$ , and  $P_{tot}$  are derived from the AI algorithm (GA+PSO), proper  $d_w$  and  $d_a$  are applied in the transformer to achieve the optimal  $L_{r1}$ ,  $L_{r2}$  and  $L_m$ .

Stages 1 and 2 will be elaborated as following.

1) *First Optimization Stage:* Using AI algorithm (GA+PSO) to optimize  $L_{r1}$ ,  $C_{r1}$ ,  $L_{r2}$ ,  $C_{r2}$ ,  $L_m$ , and  $P_{tot}$

a) Operation principles of the proposed AI algorithm (GA+PSO) in the optimal design

In this part, the AI algorithm is utilized to optimize the total power loss of the CLLC resonant converter. In the PSO algorithm, the iteration number of convergence and the global optimum contradicts each other [29]–[31]: a better global optimum always means larger iteration number while a lower iteration number always means a worse global optimum. In addition, the selection of the initial parameters and problem representation is always based on users' experience, which means the iteration number and the objective function are not optimized. As a result, in the experience-based PSO, the iteration number is sacrificed to achieve the desired accuracy. To be more specific, four parameters, *Weight.start*, *Weight.end*, *Kind*, and *Vel.max*, are main factors that determine the efficiency of the algorithm. The random selections of these four parameters will lead to the deficiency of PSO.

In this paper, a hybrid AI algorithm, named as GA+PSO, is proposed to solve the problem of high number of iterations and calculation time, which is caused by the random selection of *Weight.start*, *Weight.end*, *Kind*, and *Vel.max*. The flowchart of the proposed GA+PSO is shown in Fig. 7: Fig. 7(a) shows the overview of the proposed GA+PSO algorithm, Fig. 7(b) and (c) shows the details of the GA and PSO part, respectively.

As shown in Fig. 7(a), the proposed GA+PSO algorithm can be treated as an improved PSO, where the algorithm parameters are optimized by GA. First, the proposed GA+PSO algorithm starts from GA and the genes of each individual (*Weight.start*, *Weight.end*, *Kind*, and *Vel.max*) in GA are sent to the PSO as its algorithm parameters. With the *Weight.start*, *Weight.end*, *Kind*, and *Vel.max* from GA, the number of iterations,  $N$ , and the total power loss  $P_{tot}$  of PSO can be obtained, which will be sent back to GA to evaluate the fitness value. *Weight.start*, *Weight.end*, *Kind*, and *Vel.max* will be further optimized with the fitness value and send to PSO again. After several such recycling process between the GA and PSO, if the maximum iteration number is reached, the GA find the final optimal *Weight.start*, *Weight.end*, *Kind*, and *Vel.max* for the PSO. With optimal *Weight.start*, *Weight.end*, *Kind*, and *Vel.max*, the PSO will be executed to calculate the final optimal  $L_{r1}$ ,  $C_{r1}$ ,  $L_{r2}$ ,  $C_{r2}$ ,  $L_m$ , and  $P_{tot}$ , which are also the outputs of the proposed GA+PSO algorithm.

The proposed GA+PSO algorithm performs the following sequential tasks:

*Step 1. Initialization of GA:* The parameters of GA, including the number of individuals, the crossover rate, the starting mutation rate, the ending mutation rate, and the maximum iteration number, are initialized. The GA optimizer encodes the parameters of PSO, *Weight.start*, *Weight.end*, *Kind*, and *Vel.max*, as genes, creates a string of genes to form a chromosome, and initializes a starting population.

*Step 2. Invoking PSO to obtain the number of iterations and best  $P_{tot}$  (PSO):* *Weight.start*, *Weight.end*, *Kind*, and *Vel.max*, are transferred from GA to PSO. With the parameters from each individual in GA, PSO is executed to extract  $N$  and  $P_{tot}$ , which will be used to evaluate the fitness value of GA.

In this step, in order to achieve wide range high efficiency, when the average function value is stable or the *Max.Iteration* is reached,  $P_{tot}$  will be further checked to achieve wide-range high

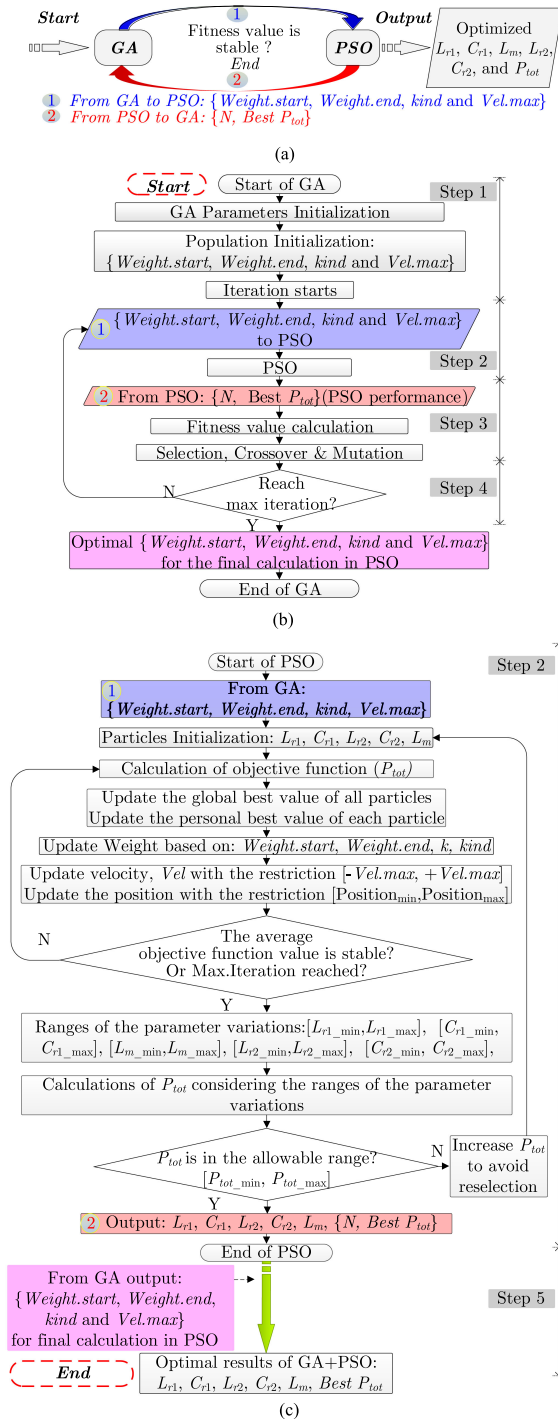


Fig. 7. Proposed recycling GA + PSO. (a) Structure diagram. (b) Flowchart of GA. (c) Flowchart of PSO.

efficiency. Considering the variations of the parameters, which are shown in Table I, if  $P_{tot}$  is still in the allowable range, which is from  $P_{tot\_min}$  to  $P_{tot\_max}$ , the circuit parameters,  $N$  and best  $P_{tot}$  will be finally confirmed. Otherwise, a large value will be assigned to  $P_{tot}$  to avoid reselection of the circuit parameters.

The details of PSO can be found from Fig. 7(c).

*Step 3. Evaluation and evolution (GA):*  $N$  and  $P_{tot}$ , derived from PSO, are used to evaluate the fitness value of GA. Based

TABLE I  
PARAMETER VARIATIONS OF THE CLLC RESONANT CONVERTER

Parameter	Range	Parameter	Range
$L_{r1}$	$[L_{r1\_min}, L_{r1\_max}]$	$L_{r2}$	$[L_{r2\_min}, L_{r2\_max}]$
$C_{r1}$	$[C_{r1\_min}, C_{r1\_max}]$	$C_{r2}$	$[C_{r2\_min}, C_{r2\_max}]$
$L_m$	$[L_m\_min, L_m\_max]$		

TABLE II  
PARAMETERS OF CLLC RESONANT CONVERTER FOR VALIDATION

Parameters of the main circuit			
$V_L$	200 V	$f_s$	90 kHz
$V_H$	200 V	$P_H$	500 W
Magnetic core (ELP 64/10/50, N87)			
$V_e$	83000 mm <sup>3</sup>	$a$	4.823
$A_e$	1038 mm <sup>2</sup>	$\beta$	5.521
$k_c$	$3.716 \times 10^{-24}$		4.823
Main switches and rectifiers (C2M0080120D)			
$V_{gs}$	20.0 V	$R_{on}$	80 mΩ
$Q_g$	62 nC	$C_{oss}$	80 pF

on the fitness value derived from PSO, the population in GA evolves, including selection, crossover and mutation.

*Step 4. Repeat Steps 2 and 3 to obtain optimal Weight.start, Weight.end, Kind, and Vel.max:* Steps 2 to 3 are repeated until the maximum iteration number of GA is reached.

*Step 5. Calculations of the optimal design parameters for the CLLC resonant converter (PSO):* With the optimal Weight.start, Weight.end, Kind, and Vel.max, the CLLC resonant converter is optimized and optimal  $L_{r1}$ ,  $C_{r1}$ ,  $L_{r2}$ ,  $C_{r2}$ ,  $L_m$ , and  $P_{tot}$  are derived.

When all the optimal parameters are derived, the optimal design process is completed.

b) Evaluation of the proposed AI algorithm (GA+PSO) in the optimal design

In this part, an example is given to validate the proposed AI based two-stage optimal design method. The parameters of the CLLC resonant converter, magnetic core, and the main switches are listed in Table II. The optimal  $L_{r1}$ ,  $L_{r2}$ ,  $C_{r1}$ ,  $C_{r2}$ , and  $P_{tot}$  are calculated by the proposed GA + PSO.  $P_{tot}$  is appointed as the objective function. The range of  $L_{r1}$  is from 10  $\mu$ H to 50  $\mu$ H; the range of  $L_m$  is from 100  $\mu$ H to 2 mH; the range of  $C_{r1}$  is from 50 to 200 nF.

In order to compare the proposed GA+PSO with other algorithms, the optimal design is carried out with GA, PSO, SA, ACO, BCO, AIS, and the proposed GA+PSO. The variations of the total loss with the number of iterations using GA, PSO, SA, ACO, BCO, AIS, and the proposed GA+PSO, are shown in Fig. 8.

The iteration number and the optimal total power loss of each optimal design method are summarized in Table III.

It can be seen from Table III that except SA, whose optimal total power loss is 14.52 W, other optimal design methods converge to the approximately same value, which is 13.76 W. However, it can be concluded that the iteration number of the proposed GA+PSO is much less than other optimal design methods.

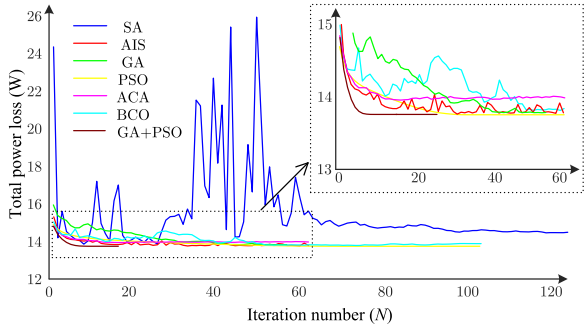


Fig. 8. Variation of the total power loss with the iteration number.

TABLE III

ITERATION NUMBER AND THE OPTIMAL TOTAL POWER LOSS OF EACH OPTIMAL DESIGN METHOD

Optimal design method	Iteration number	Optimal total power loss
SA	85	14.52 W
AIS	37	13.75 W
GA	57	13.76 W
PSO	33	13.76 W
ACA	54	13.82 W
BCO	46	13.75 W
GA+PSO	9	13.76 W

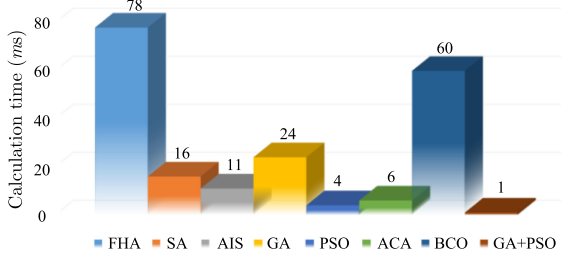


Fig. 9. Calculation time comparison.

TABLE IV

OPTIMAL PARAMETERS OF THE CLLC RESONANT CONVERTER FROM THE PROPOSED GA+PSO ALGORITHM

$L_{r1}$	$14.8 \mu\text{H}$	$C_{r1}$	$196.0 \text{ nF}$
$L_{r2}$	$14.8 \mu\text{H}$	$C_{r2}$	$196.0 \text{ nF}$
$L_m$	$1.0 \text{ mH}$		

Besides the iteration number, the calculation time of the regular First Harmonic Approximation (FHA), SA, AIS, GA, PSO, ACA, BCO, and the proposed GA+PSO is also compared, which is shown in Fig. 9. It can be concluded that compared with other optimal design methods, the proposed GA+PSO optimal design method enjoys the least calculation time.

Based on the comparison of the iteration number and the calculation time above, it can be concluded that the proposed GA+PSO algorithm has better performance compared with FHA, GA, PSO, SA, ACO, BCO, and AIS.

c) Final Optimal results of  $L_{r1}$ ,  $L_{r2}$ ,  $L_m$ ,  $C_{r1}$ ,  $C_{r2}$ , and  $P_{\text{tot}}$

With the above AI (GA+PSO) algorithm, the optimal  $L_{r1}$ ,  $L_{r2}$ ,  $L_m$ ,  $C_{r1}$ ,  $C_{r2}$ , and  $P_{\text{tot}}$  can be obtained, which are shown in Table IV. It can be seen from Table IV that,  $L_{r1} = 14.8 \mu\text{H}$ ,

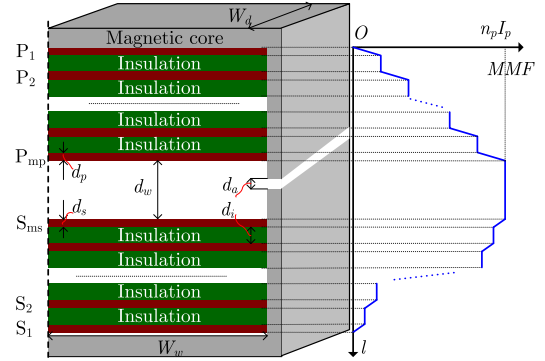


Fig. 10. General winding configuration and MMF distribution.

$C_{r1} = 196.0 \text{ nF}$ ,  $L_m = 1.0 \text{ mH}$ , and the optimal power loss  $P_{\text{tot}} = 13.76 \text{ W}$ . It is worth pointing out that  $C_{r1}$  and  $C_{r2}$  are discrete capacitors and their values can be easily designed to  $196.0 \text{ nF}$ . However,  $L_{r1}$ ,  $L_{r2}$ , and  $L_m$  are the parasitic parameters of the transformer, which are determined by the transformer winding configurations. Therefore, in the following part, a transformer with the desired parasitic parameters will be designed.

2) Second Optimization Stage: optimal design of the transformer to achieve the optimal parasitic parameters derived from AI algorithm via hybrid electromagnetic analysis

a) Derivation of the leakage inductances

Nowadays, the power converters are developing toward high efficiency and high power density. In this paper, in order to increase the power density by reducing the number of the magnetic components, the leakage inductances of the planar transformer are utilized as the resonant inductances ( $L_{r1}$  and  $L_{r2}$ ). In this part, the optimized  $L_{r1}$  and  $L_{r2}$  are achieved by designing the thickness of the primary winding and secondary winding,  $d_p$  and  $d_s$ , the thickness of the insulation, ( $d_i$ ), and the distance between the primary winding and the secondary winding ( $d_w$ ). A general equation to calculate  $d_w$  to achieve the desired the leakage inductances for the CLLC resonant converter is derived.

The winding configuration of a planar transformer and its corresponding magneto-motive force (MMF) are shown in Fig. 10. The primary winding has  $n_p$  turns, which are distributed in  $m_p$  layers while the secondary winding has  $n_s$  turns, which are distributed in  $m_s$  layers. The distance between the primary winding and the secondary winding is  $d_w$ , which will be calculated to achieve the optimal leakage inductances. The air gap ( $d_a$ ) is added to achieve the desired magnetizing inductances.

Assuming the current excitation to the primary winding is  $I_p$ , based on the distribution MMF in Fig. 10, the magnetic energy stored in the core window can be calculated by

$$E_m = \frac{\mu_0 \mu_r n_p^2 I_p^2 W_d}{6W_w} \left[ 2m_p d_p + 2m_s d_s + \frac{(m_p - 1)(2m_p - 1)}{m_p} d_i + \frac{(m_s - 1)(2m_s - 1)}{m_s} d_i + 6d_w \right] \quad (29)$$

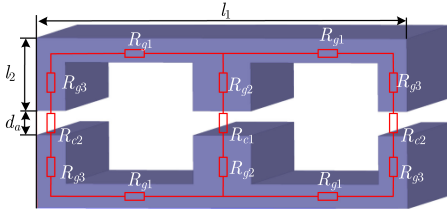


**Fig. 11.** Equivalent magnetic circuit of a planar transformer with an air gap.

where  $W_d$  is the depth of the window,  $W_w$  is the width of the window.

According to the relation between leakage inductance and magnetic energy [36]–[38], the leakage inductances can be calculated by

$$\begin{aligned} L_{lk1} = L_{lk2} = \frac{\mu_0 \mu_r n_p^2 W_d}{6W_w} & [2m_p d_p + 2m_s d_s \\ & + \frac{(m_p - 1)(2m_p - 1)}{m_p} d_i + \frac{(m_s - 1)(2m_s - 1)}{m_s} d_i + 6d_w]. \end{aligned} \quad (30)$$

As a result, it can be concluded from (30) that the optimal leakage inductances can be achieved by changing  $d_w$ .

The distance between primary winding and the secondary winding,  $d_w$ , which is used to achieve the desired leakage inductance, can be calculated by

$$\begin{aligned} d_w = \frac{W_w L_{lk1}}{\mu_0 \mu_r n_p^2 W_d} - \frac{m_p d_p}{3} - \frac{m_s d_s}{3} - \frac{(m_p - 1)(2m_p - 1)}{6m_p} d_i \\ - \frac{(m_s - 1)(2m_s - 1)}{6m_s} d_i. \end{aligned} \quad (31)$$

### b) Derivation of the magnetizing inductance

In order to achieve the desired magnetizing inductance, the thickness of the air gap ( $d_a$ ) is adjusted. In this part, the equation to calculate the thickness of the air gap ( $d_a$ ) to achieve the desired magnetizing inductance ( $L_m$ ) is derived. The 3-D model of a planar transformer with an air gap and its corresponding equivalent magnetic circuit is shown in Fig. 11.

The magnetic reluctances,  $R_{g1}$ ,  $R_{g2}$ ,  $R_{g3}$ ,  $R_{c1}$ , and  $R_{c2}$  can be calculated by

$$R_{g1} = l_1 / (\mu_0 \mu_r A_e) \quad (32a)$$

$$R_{g2} = l_2 / (\mu_0 \mu_r A_e) \quad (32b)$$

$$R_{g3} = 2l_2 / (\mu_0 \mu_r A_e) \quad (32c)$$

$$R_{c1} = d_a / (\mu_0 A_e) \quad (32d)$$

$$R_{c2} = 2d_a / (\mu_0 A_e) \quad (32e)$$

where  $l_1$  and  $l_2$  are the dimensions of the magnetic core, which can be found in Fig. 11.  $A_e$  is the cross-sectional area of the centre leg.

As a result, the magnetizing inductance can be calculated by

$$L_m = \mu_0 \mu_r A_e n_p^2 / (l_1 + 4l_2 + 3\mu_r d_a). \quad (33)$$

**TABLE V**  
PARAMETERS OF THE MAGNETIC CORE

$n_p$	16	$d_i$	0.1 mm
$n_s$	16	$W_w$	22 mm
$m_p$	4	$W_d$	100 mm
$m_s$	4	$A_e$	1038 mm <sup>2</sup>
$d_p, d_s$	70 $\mu\text{m}$	$l_1$	64 mm
$\mu_r$	1490	$l_2$	10 mm

Based on (33), it can be concluded that with higher  $d_a$ , the magnetizing inductances will decrease. As a result, by changing  $d_a$ , the optimal  $L_m$  can be achieved.

The thickness of the air gap,  $d_a$ , which is used to achieve the desired  $L_m$ , can be calculated by

$$d_a = (\mu_0 A_e n_p^2) / (3L_m) - (l_1 + 4l_2) / (3\mu_r). \quad (34)$$

## IV. SIMULATION AND EXPERIMENTAL VALIDATIONS OF THE AI-BASED TWO-STAGE OPTIMAL DESIGN METHOD

In this section, the proposed AI-based optimal design method is validated by simulations and experiments. In the first part, with the equations of  $d_w$  and  $d_a$ , the planar transformer for the CLLC resonant converter is built. In addition, the hybrid electromagnetic field simulations are carried out to validate the calculations. In the second part, the CLLC resonant converter with the planar transformer is tested to validate the proposed two-stage optimal design method.

### A. Design of a Planar Transformer With the Desired Parasitic Parameters for a CLLC Resonant Converter

Considering the output power, the magnetic core, ELP 64/10/50, with N87 as the magnetic material from TDK is selected. In order to increase the power capacity, two ELP 64/10/50 are combined to increase  $A_e$ . The parameters of the magnetic core are listed in Table V.

The parameters in Table V will be used for the design of the planar transformer for the CLLC resonant converter.

**1) Design of a Planar Transformer Based on (31) and (34):** In order to achieve the optimized parameters shown in Table IV,  $d_w$  and  $d_a$  can be calculated by (31) and (34), which are

$$d_w = 9.15 \text{ mm} \quad (35a)$$

$$d_a = 0.14 \text{ mm}. \quad (35b)$$

The calculated  $d_w$  and  $d_a$  will be validated by the hybrid electromagnetic simulations.

### 2) Hybrid Electromagnetic Field Simulation Validation:

The planar transformer model with the calculated  $d_w$  and  $d_a$  is built in Ansys Maxwell and the hybrid electromagnetic field simulations are carried out to validate the effectiveness of the calculations. The distributions of magnetic flux density for calculating the leakage inductances and magnetizing inductance are shown in Fig. 12(a) and (b), respectively. Based on Fig. 12, the simulated  $L_{r1}$ ,  $L_{r2}$ , and  $L_m$  are shown in Table VI.

The planar transformer with the calculated  $d_w$  and  $d_a$  for the CLLC resonant converter is built, which is shown in Fig. 13.

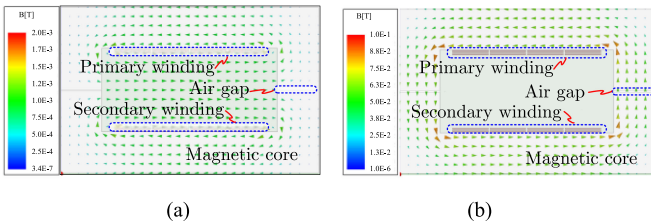


Fig. 12. Distribution of magnetic flux density for calculations of (a) leakage inductance and (b) magnetizing inductance.

TABLE VI  
COMPARISON OF LEAKAGE INDUCTANCES AND MAGNETIZING INDUCTANCE

Parameters	Optimal	Simulated	Measured
$L_{r1}$ ( $\mu\text{H}$ )	14.8	14.38	14.73
$L_{r2}$ ( $\mu\text{H}$ )	14.8	14.38	14.73
$L_m$ (mH)	1.0	1.02	1.03

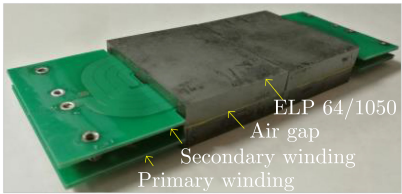


Fig. 13. Planar transformer for the CLLC resonant converter.

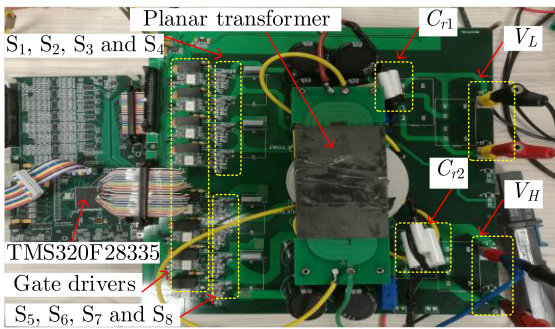


Fig. 14. CLLC resonant converter for the validation.

Besides,  $L_{r1}$ ,  $L_{r2}$ , and  $L_m$  are also measured by the impedance analyser and the measured results are shown in Table VI as well.

It can be seen from Table VI that the simulated and measured results agree with the calculated results, which validates the effectiveness of (31) and (34). In the following part, the planar transformer will be tested in the CLLC resonant converter to further validate the proposed two-stage optimal design method.

### B. Experimental Validation of the Proposed AI-Based Two-Stage Optimal Design Methodology

As shown in Fig. 14, the CLLC resonant converter, where the designed planar transformer is used, is built to validate the proposed AI-based two-stage optimal design method.

**1) Soft-Switching Verifications of the CLLC Resonant Converter:** In order to show the ZVS of the switches, the

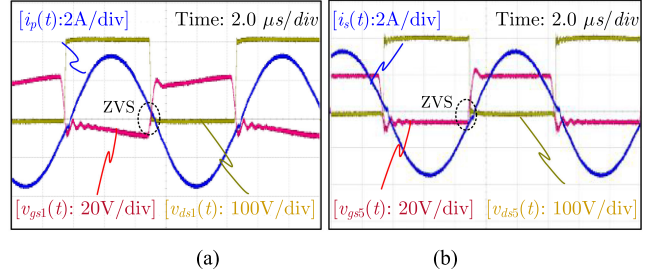


Fig. 15. Experimental waveforms of  $S_1$  and  $S_5$  to validate the soft-switching characteristics. (a)  $S_1$ . (b)  $S_5$ .

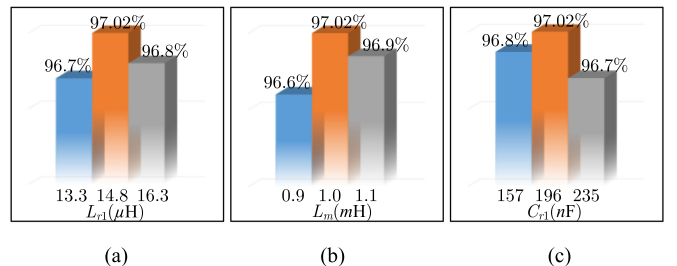


Fig. 16. Comparison of efficiency under different resonant parameters. (a)  $L_{r1}$ . (b)  $L_m$ . (c)  $C_{r1}$ .

experiments are carried out and the driving signals of  $S_1$  and  $S_5$ ,  $v_{gs1}(t)$  and  $v_{gs5}(t)$ , the primary current and the secondary current,  $i_p(t)$  and  $i_s(t)$ , the voltages of  $S_1$  and  $S_5$ ,  $v_{ds1}(t)$ , and  $v_{ds5}(t)$ , are shown in Fig. 15.

It can be seen from Fig. 15(a) that before  $S_1$  is turned-ON, the voltage of  $S_1$ ,  $v_{ds1}(t)$  has decreased to 0. As a result, when  $S_1$  is turned-ON, ZVS of  $S_1$  is achieved. Similar to  $S_1$ ; it can be seen from Fig. 15(b) that before  $S_5$  is turned-ON, the voltage of  $S_5$ ,  $v_{ds5}(t)$  has decreased to 0. As a result, when  $S_5$  is turned-ON, ZVS of  $S_5$  is achieved. The experimental results are in accordance with the theoretical analysis.

### 2) Efficiency Verification of the AI-Based Optimal Design Method

**Method:** In order to validate the effectiveness of the proposed design methodology, considering the variations of the real resonant parameters, the cases where  $L_{r1}$ ,  $L_m$ , and  $C_{r1}$  deviate from their corresponding optimal design values are tested. For the resonant inductors,  $L_{r1}$  and  $L_m$ , the efficiencies when the inductances varying by 10% are measured, which are shown in Fig. 16(a) and (b), respectively. For the resonant capacitance,  $C_{r1}$ , the efficiency when it varies by 20% is measured, which is shown in Fig. 16(c).

It can be seen from Fig. 16 that the efficiency of the CLLC resonant converter is affected by  $L_{r1}$ ,  $L_m$ , and  $C_{r1}$ . However, under the optimal condition, the efficiency is higher than other cases, which validates the effectiveness of the proposed two-stage optimal design method in this paper.

**3) Efficiency Under Different Output Power:** The waveforms of input voltage and input current,  $V_L$ ,  $i_L$ , output voltage and output current,  $V_H$ , and  $i_H$  are shown in Fig. 17. The efficiency of the CLLC resonant converter is measured under different output power, which is shown in Fig. 18. It can be seen from Fig. 18 that at rated output power (500 W), the efficiency

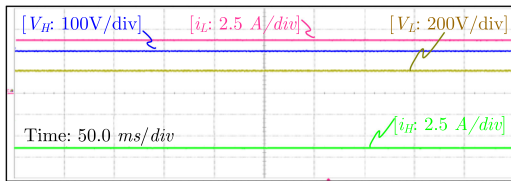


Fig. 17. Waveforms of  $V_L$ ,  $V_H$ ,  $i_L$ , and  $i_H$ .

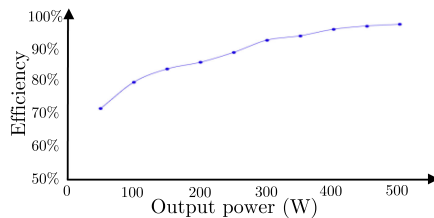


Fig. 18. Efficiency of the CLLC resonant converter versus output power.

is up to 97.02%. Under rated output power, the measured total power loss is 14.92 W, which is also in accordance with the optimal design result (13.76 W).

## V. CONCLUSION

An AI (GA+PSO)-based two-stage optimal design methodology of high-efficiency CLLC resonant converters for the hybrid ac–dc microgrid applications was proposed in this paper. The proposed method focused on the total power optimization of the open-loop CLCL resonant converter with AI algorithm and the corresponding magnetic design. In the first stage, the total power loss, including the driving loss, conduction loss of the switches, power loss of the resonant capacitances, copper loss of the transformer, and core loss of the transformer, was optimized by the GA+PSO algorithm and the optimized  $L_{r1}$ ,  $L_{r2}$ ,  $C_{r1}$ ,  $C_{r2}$ , and  $L_m$  were derived. In the second stage, to realize the AI optimal design, planar transformer with optimal  $L_{r1}$ ,  $L_{r2}$ , and  $L_m$  was designed. The proposed optimal design method has been validated by an example.

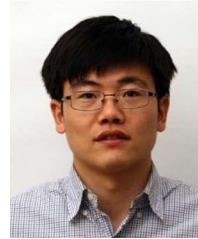
Besides the optimal design methodology, the planar transformer design for the CLLC resonant converter was also been investigated. General equations to calculate the thickness of the air gap and the distance between the primary and secondary winding was proposed. With the proposed equations, the thickness of the air gap and the distance between the primary winding and the secondary winding could be easily calculated. Both the hybrid electromagnetic simulations and the experimental results validated the proposed equations.

It may be concluded that the AI algorithm can be used to solve the total power loss optimization despite the challenges caused by multiple circuit variables and their internal couplings. In addition, it is worthy to point out that the application of the AI algorithm on the optimal design of the power converter mainly contains two challenging parts: the first part is the optimization of the power converter with AI algorithms to derive the optimal circuit parameters and the second part is the realization of the optimal circuit parameters.

## REFERENCES

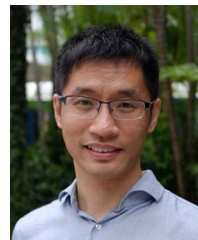
- [1] Y. Xia, W. Wei, M. Yu, X. Wang, and Y. Peng, "Power management for a hybrid AC/DC microgrid with multiple subgrids," *IEEE Trans. Power Electron.*, vol. 33, no. 4, pp. 3520–3533, Apr. 2018.
- [2] X. Zhang, Q. Zhong, V. Kadirkamanathan, J. He, and J. Huang, "Source-side series-virtual-impedance control to improve the cascaded system stability and the dynamic performance of its source converter," *IEEE Trans. Power Electron.*, vol. 34, no. 6, pp. 5854–5866, Jun. 2019.
- [3] Y. Xia, Y. Peng, P. Yang, M. Yu, and W. Wei, "Distributed coordination control for multiple bidirectional power converters in a hybrid AC/DC microgrid," *IEEE Trans. Power Electron.*, vol. 32, no. 6, pp. 4949–4959, Jun. 2017.
- [4] F. Nejabatkhah and Y. W. Li, "Overview of power management strategies of hybrid AC/DC microgrid," *IEEE Trans. Power Electron.*, vol. 30, no. 12, pp. 7072–7089, Dec. 2015.
- [5] N. Eghdarpour and E. Farjah, "Power control and management in a hybrid AC/DC microgrid," *IEEE Trans. Smart Grid*, vol. 5, no. 3, pp. 1494–1505, May 2014.
- [6] P. He and A. Khaligh, "Comprehensive analyses and comparison of 1 kW isolated DC–DC converters for bidirectional EV charging systems," *IEEE Trans. Transport. Electrific.*, vol. 3, no. 1, pp. 147–156, Mar. 2017.
- [7] S. Zhao, Q. Li, F. C. Lee, and B. Li, "High-frequency transformer design for modular power conversion from medium-voltage AC to 400 VDC," *IEEE Trans. Power Electron.*, vol. 33, no. 9, pp. 7545–7557, Sep. 2018.
- [8] X. Zhang and Q. Zhong, "Improved adaptive-series-virtual-impedance control incorporating minimum ripple point tracking for load converters in DC systems," *IEEE Trans. Power Electron.*, vol. 31, no. 12, pp. 8088–8095, Dec. 2016.
- [9] B. Zhao, Q. Song, W. Liu, and Y. Sun, "Overview of dual-active-bridge isolated bidirectional DC–DC converter for high-frequency-link power-conversion system," *IEEE Trans. Power Electron.*, vol. 29, no. 8, pp. 4091–4106, Aug. 2014.
- [10] J. H. Jung, H. S. Kim, M. H. Ryu, and J. W. Baek, "Design methodology of bidirectional CLLC resonant converter for high-frequency isolation of DC distribution systems," *IEEE Trans. Power Electron.*, vol. 28, no. 4, pp. 1741–1755, Apr. 2013.
- [11] Z. U. Zahid, Z. M. Dalala, R. Chen, B. Chen, and J. S. Lai, "Design of bidirectional DC–DC resonant converter for vehicle-to-grid (V2G) applications," *IEEE Trans. Transport. Electrific.*, vol. 1, no. 3, pp. 232–244, Oct. 2015.
- [12] J. Huang *et al.*, "Robust circuit parameters design for the CLLC-type DC transformer in the hybrid AC/DC microgrid," *IEEE Trans. Ind. Electron.*, vol. 66, no. 3, pp. 1906–1918, Mar. 2019.
- [13] C. Zhang, P. Li, Z. Kan, X. Chai, and X. Guo, "Integrated half-bridge CLLC bidirectional converter for energy storage systems," *IEEE Trans. Ind. Electron.*, vol. 65, no. 5, pp. 3879–3889, May 2018.
- [14] W. L. Malan, D. M. Vilathgamuwa, and G. R. Walker, "Modeling and control of a resonant dual active bridge with a tuned CLLC network," *IEEE Trans. Power Electron.*, vol. 31, no. 10, pp. 7297–7310, Oct. 2016.
- [15] S. Zou, J. Lu, A. Mallik, and A. Khaligh, "Bidirectional CLLC converter with synchronous rectification for plug-in electric vehicles," *IEEE Trans. Ind. Appl.*, vol. 54, no. 2, pp. 998–1005, Mar./Apr. 2018.
- [16] G. Liu, D. Li, J. Q. Zhang, B. Hu, and M. L. Jia, "Bidirectional CLLC resonant DC–DC converter with integrated magnetic for OBCM application," in *Proc. IEEE Int. Conf. Ind. Technol.*, Seville, Spain, 2015, pp. 946–951.
- [17] S. Zou, J. Lu, A. Mallik, and A. Khaligh, "Modeling and optimization of an integrated transformer for electric vehicle onboard charger applications," *IEEE Trans. Transport. Electrific.*, vol. 4, no. 2, pp. 355–363, Jun. 2018.
- [18] B. Li, Q. Li, and F. C. Lee, "A WBG-based three phase 12.5 kW 500 kHz CLLC resonant converter with integrated PCB winding transformer," in *Proc. IEEE Appl. Power Electron. Conf. Expo.*, San Antonio, TX, USA, 2018, pp. 469–475.
- [19] S. Zhao, Q. Li, F. C. Lee, and B. Li, "High frequency transformer design for modular power conversion from medium voltage AC to 400 V DC," *IEEE Trans. Power Electron.*, vol. 33, no. 9, pp. 7545–7557, Sep. 2018.
- [20] P. He, A. Mallik, A. Sankar, and A. Khaligh, "Design of a 1-MHz high-efficiency high-power-density bidirectional GaN-based CLLC converter for electric vehicles," *IEEE Trans. Veh. Technol.*, vol. 68, no. 1, pp. 213–223, Jan. 2019.
- [21] S. E. De León-Aldaco, H. Calleja, and J. Aguayo Alquicira, "Metaheuristic optimization methods applied to power converters: A review," *IEEE Trans. Power Electron.*, vol. 30, no. 12, pp. 6791–6803, Dec. 2015.

- [22] Y. Wang, F. Li, Q. Wan, and H. Chen, "Reactive power planning based on fuzzy clustering, gray code, and simulated annealing," *IEEE Trans. Power Syst.*, vol. 26, no. 4, pp. 2246–2255, Nov. 2011.
- [23] R. Liu and L. Li, "Simulated annealing algorithm coupled with a deterministic method for parameter extraction of energetic hysteresis model," *IEEE Trans. Magn.*, vol. 54, no. 11, pp. 1–5, Nov. 2018, Art no. 7301105.
- [24] Z. Yin, C. Du, J. Liu, X. Sun, and Y. Zhong, "Research on auto disturbance-rejection control of induction motors based on an ant colony optimization algorithm," *IEEE Trans. Ind. Electron.*, vol. 65, no. 4, pp. 3077–3094, Apr. 2018.
- [25] Y. Zhou, "Runtime analysis of an ant colony optimization algorithm for TSP instances," *IEEE Trans. Evol. Comput.*, vol. 13, no. 5, pp. 1083–1092, Oct. 2009.
- [26] A. Karaarslan, "The implementation of bee colony optimization algorithm to Sheppard–Taylor PFC converter," *IEEE Trans. Ind. Electron.*, vol. 60, no. 9, pp. 3711–3719, Sep. 2013.
- [27] F. S. Abu-Mouti and M. E. El-Hawary, "Optimal distributed generation allocation and sizing in distribution systems via artificial bee colony algorithm," *IEEE Trans. Power Del.*, vol. 26, no. 4, pp. 2090–2101, Oct. 2011.
- [28] X. Hao and S. Cai-xin, "Artificial immune network classification algorithm for fault diagnosis of power transformer," *IEEE Trans. Power Del.*, vol. 22, no. 2, pp. 930–935, Apr. 2007.
- [29] K. Ishaque and Z. Salam, "A deterministic particle swarm optimization maximum power point tracker for photovoltaic system under partial shading condition," *IEEE Trans. Ind. Electron.*, vol. 60, no. 8, pp. 3195–3206, Aug. 2013.
- [30] M. A. Hassan and M. A. Abido, "Optimal design of microgrids in autonomous and grid-connected modes using particle swarm optimization," *IEEE Trans. Power Electron.*, vol. 26, no. 3, pp. 755–769, Mar. 2011.
- [31] M. Veerachary and A. R. Saxena, "Optimized power stage design of low source current ripple fourth-order boost DC–DC converter: A PSO approach," *IEEE Trans. Ind. Electron.*, vol. 62, no. 3, pp. 1491–1502, Mar. 2015.
- [32] X. Lai, P. Zhang, Y. Wang, and M. Wu, "Position-posture control of a planar four-link underactuated manipulator based on genetic algorithm," *IEEE Trans. Ind. Electron.*, vol. 64, no. 6, pp. 4781–4791, Jun. 2017.
- [33] K. Sundareswaran and V. T. Sreedevi, "Boost converter controller design using queen-bee-assisted GA," *IEEE Trans. Ind. Electron.*, vol. 56, no. 3, pp. 778–783, Mar. 2009.
- [34] A. Garcia-Bediaga, I. Villar, A. Rujas, L. Mir, and A. Rufer, "Multiobjective optimization of medium-frequency transformers for isolated soft-switching converters using a genetic algorithm," *IEEE Trans. Power Electron.*, vol. 32, no. 4, pp. 2995–3006, Apr. 2017.
- [35] J. Huang, J. Xiao, C. Wen, P. Wang, and A. Zhang, "Implementation of bidirectional resonant DC transformer in hybrid AC/DC microgrid," *IEEE Trans. Smart Grid*, vol. 10, no. 2, pp. 1532–1542, Mar. 2019.
- [36] B. Zhao, Z. Ouyang, M. Duffy, M. A. E. Andersen, and W. G. Hurley, "An improved partially interleaved transformer structure for high-voltage high-frequency multiple-output applications," *IEEE Trans. Ind. Electron.*, vol. 66, no. 4, pp. 2691–2702, Apr. 2019.
- [37] Z. Ouyang, J. Zhang, and W. G. Hurley, "Calculation of leakage inductance for high-frequency transformers," *IEEE Trans. Power Electron.*, vol. 30, no. 10, pp. 5769–5775, Oct. 2015.
- [38] W. Tan, X. Margueron, L. Taylor, and N. Idir, "Leakage inductance analytical calculation for planar components with leakage layers," *IEEE Trans. Power Electron.*, vol. 31, no. 6, pp. 4462–4473, Jun. 2016.



**Bin Zhao** (M'18) received the B.S. degree in electrical engineering from Nanjing Agricultural University, Nanjing, China, in 2012, and the Ph.D. degree in electronic and electrical engineering from the Institute of Electronics, Chinese Academy of Sciences, Beijing, China, in 2017.

From 2015 to 2016, he was a Visiting Scholar with the National University of Ireland, Galway, Ireland. From 2017 to 2018, he was a Postdoc Researcher with the Department of Electrical Engineering, Technical University of Denmark. From 2018 to 2019, he was a Research Fellow with Energy Research Institute, Nanyang Technological University. Currently he has been with the Space Travelling-Wave Tube Research & Development Center, Institute of Electronics, Chinese Academy of Sciences, as a Professor. His current research interests include high frequency magnetic simulation, design, and integration in power electronics and resonant converters.



**Xin Zhang** (M'15) received the Ph.D. degree in electronic and electrical engineering from the Nanjing University of Aeronautics & Astronautics, China, in 2014, and the Ph.D. degree in automatic control and systems engineering from the University of Sheffield, U.K., in 2016.

He is currently an Assistant Professor of Power Engineering with the School of Electrical and Electronic Engineering, Nanyang Technological University. His research interests include power electronics, power system, and advanced control theory, together with their applications in various sectors.

Dr. Zhang is an Associate Editor for the IEEE TRANSACTIONS ON INDUSTRIAL ELECTRONICS, IEEE JOURNAL OF EMERGING AND SELECTED TOPICS IN POWER ELECTRONICS, and IET Power electronics. He has received the highly-prestigious Chinese National Award for Outstanding Students Abroad in 2016.



**Jingjing Huang** (S'11–M'18) received the B.S. degree from the Henan University of Science and Technology, Luoyang, China, in 2008, and the Ph.D. degree from Xi'an Jiaotong University, Xi'an, China, in 2014, both in electrical engineering.

Since 2014, she has been working with the Xi'an University of Technology as a Lecturer of Electronic and Electrical Engineering. Since 2016, she has been working as a Postdoctoral Research Fellow in Nanyang Technological University. Her research interests include renewable energy system, high-frequency transformer, hybrid ac/dc microgrid, and high-power converters.